Title	High figure of merit nonlinear microelectromagnetic energy harvesters for wideband applications
Authors	Mallick, Dhiman;Amann, Andreas;Roy, Saibal
Publication date	2016-12-26
Original Citation	Mallick, D., Amann, A. and Roy, S. (2016) 'High figure of merit nonlinear microelectromagnetic energy harvesters for wideband applications', Journal of Microelectromechanical Systems, 26(1), pp.273-282. doi:10.1109/JMEMS.2016.2636164
Type of publication	Article (peer-reviewed)
Link to publisher's version	10.1109/JMEMS.2016.2636164
Rights	© 2016, IEEE. Personal use of this material is permitted. Permission from IEEE must be obtained for all other uses, in any current or future media, including reprinting/republishing this material for advertising or promotional purposes, creating new collective works, for resale or redistribution to servers or lists, or reuse of any copyrighted component of this work in other works.
Download date	2025-01-15 10:47:50
Item downloaded from	https://hdl.handle.net/10468/4418

High Figure of Merit Nonlinear Microelectromagnetic Energy Harvesters for Wideband Applications

Dhiman Mallick, Andreas Amann, and Saibal Roy, *Member, IEEE*

Abstract—We report a new approach for designing high-performance microelectromechanical system (MEMS) electromagnetic energy harvesting devices, which can operate at low frequency (<1 kHz) over the ultrawide bandwidth of 60–80 Hz. The output power from the devices is increased significantly at a low optimized load and this overall enhancement in performances is benchmarked using a "power integral (P_f)" figure-of-merit. The experimental results show that the efficient nonlinear designs produce large P_f values, giving rise to one of the highest normalized P_f densities among the reported MEMS scale nonlinear energy harvesting devices. This improvement is achieved by suitably designing the nonlinear spring architectures, where the nonlinearity arises from the stretching strain of the specifically designed fixed–fixed configured spring arms under large deflections and gives rise to wideband output response. Different fundamental modes of the mechanical structures are brought relatively close, which further widens the power-frequency response by topologically varying the spring architectures and by realizing the same using the thin silicon-on-insulator substrate using MEMS processing technology. In addition, we have used the magnet as proof mass to increase the output power in contrary to conventional approach of using the coil as the proof mass in micro-electromagnetic energy harvesters. The high performance obtained from the MEMS energy harvesters with integrated double layer micro-coil is compared with the same using wire wound copper coil. The experimentally obtained results are qualitatively explained by using a finite-element analysis of the designed structures.   [2016-0038]

Index Terms—MEMS, energy conversion, electromagnetics, vibration, nonlinear, power integral.

I. INTRODUCTION

T HE VISION to add internet capability in the coming decades to everything - often called the 'Internet of Things (IoT)' [1], [2], pushes the emergence of a specific technological platform which could potentially lead to a smart, connected and responsive world using billions of low power, tiny and autonomous Wireless Sensor Nodes (WSNs). However, widespread deployment of WSNs, particularly in

remote and difficult to access locations, is restrained by lack of reliable and robust power sources which can provide energy to the sensors for a longer period. This particular issue has surged the research in the last decade to study the prospect of harvesting the energy out of ambient mechanical vibrations where a Vibrational Energy Harvester (VEH) can mainly work based on three major transduction mechanism i.e. piezoelectric [3]–[5], electromagnetic [6]–[8] and electrostatic [9]–[11]. Among these techniques, Electromagnetic (EM) energy harvesters have the advantages of low output impedance and high output current levels, but the micro-scale implementation is found to be challenging due to realization of multiple-turn coils and permanent magnets using MEMS techniques. Most attempts to incorporate permanent magnets using microfabrication techniques such as sputter deposition [12], electrodeposition [13] or magnetic powder bonding [14] in EM VEH have resulted in very low output power (few pW - nW) level. In other approaches, the micro-coil is integrated on to the moving silicon paddle which experiences varying magnetic field due to the relative motion with respect to static NdFeB bulk magnets [6], [7], [21], [23], [28]. The output power is found to be low in such cases too due to poor magnetic flux linkage and smaller proof mass. Another key element for efficient EM transductions is the microfabricated pick-up coils. Liu *et al.* [28] reported an in-plane moving EM harvester where two layers of Aluminum coil is sputtered onto the movable silicon structure. The thickness of the sputtered metallic layers is normally small due to the slow deposition rate and reported sputtered metals such as Aluminium has higher resistivity than copper. Similar sputtered, double layer coil is used in other works as well [7], [23]. Eletroplated planar copper coils are previously used [6], [15] as opposed to sputtered coils in order to develop thick conducting layers. Zorlua and Külah [16] reported electroplated double layer copper coil, each layer having 41 turns, integrated on parylene cantilever. Smaller proof mass in the developed structure resulted in a high (>1 kHz) resonance frequency. Thus proper configuration of magnet and coil along with development of suitable MEMS components are essential to improve the performance of micro-electromagnetic energy harvesters.

From the mechanical structure point of view, a major part of the earlier reported works in the field of VEHs involved linear resonating structures [3], [4], [6], [8], [10], [11]. In such resonance based systems, the output response drops significantly as the external excitation frequency shifts slightly

from the natural frequency of the structure. However in a number of practical applications, the available vibration frequency is seen to vary over time or is completely random in nature. In such situations, the efficiency of the linear VEHs is extremely low. Thus in order to address this problem, a number of strategies has been reported in recent literature to improve the efficiency of the energy harvesters under frequency varying environment. Resonant frequency tuning [17]–[20], activating multiple modes [21]–[23] and nonlinear energy harvesting [24]–[32] have emerged as the prospective solutions. However not all of these techniques are suitable for integration in a Micro Electro Mechanical System (MEMS) based energy harvesting device. As a result, development of wideband MEMS VEH remains still a challenge. Due to smaller device size, fragile materials and complicated fabrication technology, the more convenient way to insert wideband capability in a MEMS device is through the suitable design of the mechanical structure. Employing multiple MEMS cantilevers with different physical dimensions to achieve separate resonance frequencies [21] or activating multiple fundamental modes of a linear structure within a close frequency range [22], [23] through design modulations are popular methods to operate under multi-frequency input. Nonlinear oscillation based on stretching strain of specially designed beams [28], [29], [31] and frequency up conversion using mechanical impacts [11], [32] are potential methods to develop wideband VEHs at MEMS scale.

In this paper, two MEMS electromagnetic energy harvesting systems are studied. The nonlinear spring architecture is varied in the two different spring structures to study the consequent effect on the wideband output response. Using suitable design choices of the spring architectures, different fundamental modes are obtained close to each other, while further widening the output response. The devices are characterized at different level of MEMS integration to obtain a comparative result. In the following sections, initially the design methodology and micro-fabrication of the devices are described. Then Finite Element Method (FEM) simulations are incorporated to study the static nonlinear and modal characteristics of the developed devices. Finally, the devices are characterized experimentally and the wideband responses are explained in terms of the FEM analysis performed.

II. Design and Microfabrication of the MEMS Electromagnetic Energy Harvesters

A. Design Configuration

Schematic drawing of the nonlinear MEMS spring structures are shown in Fig. 1. The first nonlinear architecture (A1) [Fig. 1(a)] consists of a large movable mass suspended by four fixed-guided beam arms. The arms are fixed in two opposite corners of the frame and attached pairwise to two other opposite corners of the movable paddle. The second nonlinear spring architecture (A2) [Fig. 1(b)] consists of a pair of fixed-fixed beams which form an H-shaped configuration. The large movable mass along with the thin beam joints act as the middle bar of the 'H' in this case. For both the spring architectures, the thickness and width of the beam arms are 50 μm and 200 μm
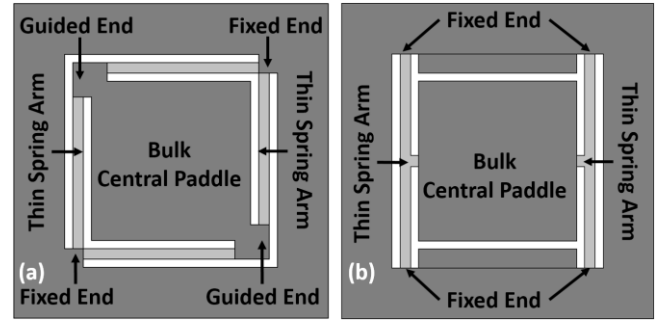

Fig. 1. Schematic of the nonlinear spring architectures (a) Nonlinear Acrchitecture 1 (A1) and (b) Nonlinear Architecture 2 (A2). The light grey represents the thin silicon spring arms whereas the dark grey denotes the bulk silicon-on-insulator.

TABLE I
DIFFERENT DESIGN PARAMETERS OF THE TWO NONLINEAR SPRING ARCHITECTURES

Parameters	Nonlinear Architecture 1 (A1)	Nonlinear Architecture 2 (A2)
Length of a beam from a fixed to guided end (mm)	2.85	1.9
Angle between fixed-fixed ends (degree)	90	0
Width of the beams (mm)	0.2	0.2
Thickness of the beams (μm)	50	50
Dimension of movable paddle (mm^3)	3×3×0.5	3×3×0.5
Mass attached (magnet) (kg)	9.83×10^{-5}	9.83×10^{-5}

respectively whereas the movable paddles have dimension of $3 \times 3 \times 0.5$ mm respectively. Detailed dimensions of the two nonlinear spring designs are provided in Table I. The movable spring structures are fabricated using MEMS fabrication techniques. Double layer electroplated copper coils are fabricated on a separate Silicon substrate, which consist of two layers of copper coils with the coil track width, the inter-track gap and the height of each of the coil being 10 μm each. The square shaped coil has an outer dimension of 2.8×2.8 mm^2. Each of the microfabricated double layer coils has 144 turns with the coil resistance of 192 Ω. The MEMS spring structure and coil are packaged together to form the nonlinear microelectromagnetic energy harvesting devices. A small NdFeB block magnet ($2.5 \times 2.5 \times 2$ mm^3) is epoxy bonded onto the movable paddle which provides mass (9.83×10^{-5} Kg) to the vibrating oscillator.

Initially, the batch fabricated and diced nonlinear spring structures are packaged with commercially available wire wound copper coils having comparable dimensions to that of the micro-fabricated copper coils. The circular wire wound coil with 3mm outer diameter, 0.5 mm thickness and 25 μm wire diameter, has 560 turns and a coil resistance of 140 Ω. Two experimental prototypes with each of the MEMS spring architectures are shown in Fig. 2(a) and Fig. 2(b) respectively, where each device has a volume of 0.14 cm^3. The cross-sectional schematic of the packaged MEMS devices is shown
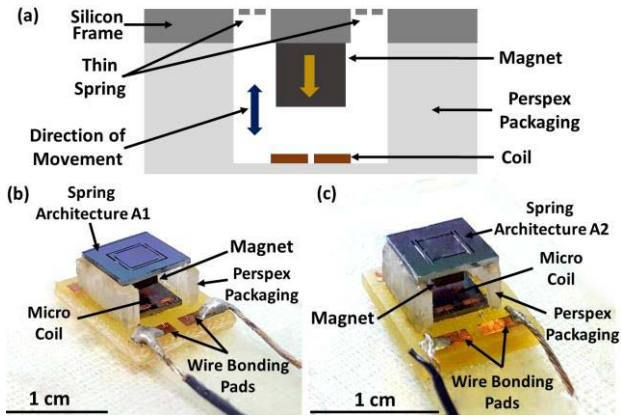
Fig. 2. (a) Cross-sectional view of the packaged devices. Packaged nonlinear MEMS electromagnetic energy harvesting devices (b) device with A1 architecture and (c) device with A2 architecture.
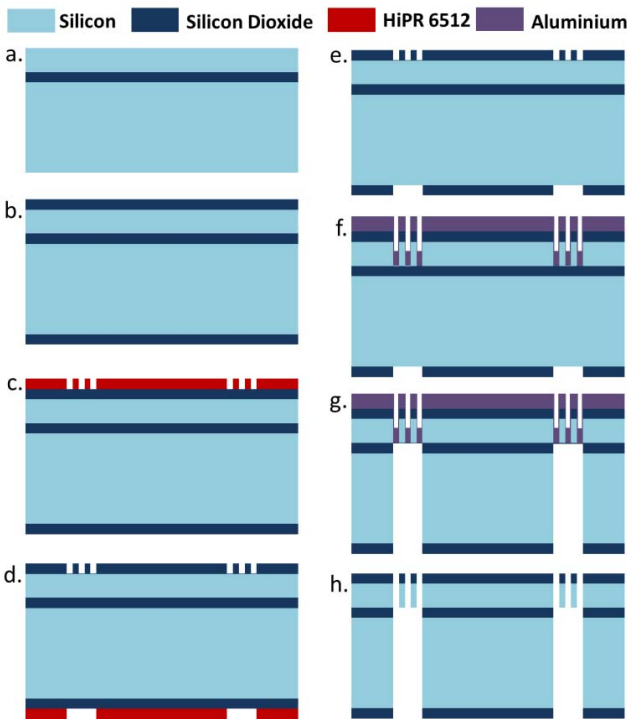

Fig. 3. Process flow for fabrication of MEMS nonlinear spring structures: (a) silicon-on-Insulator (SOI) substrate; (b) oxide mask layer deposition; (c) front side photoresist patterning; (d) front oxide layer etching and back side photoresist patterning; (e) back oxide layer etching; (f) device layer DRIE etching and Al layer sputtering; (g) handle and BOX layer DRIE etching; (h) wet etching of Sputtered Al layer.

in Fig. 2(c). An acrylic spacer is used to create a gap of 1 mm between the moving magnet and the fixed coil of the device to allow relative motion between the two.

B. Microfabrication

Fig. 3 shows cross-sectional views of the microfabrication process flow of the nonlinear architectures as indicated in Fig. 2(a). The process starts with a 500 μm thick, double side polished Silicon-On-Insulator (SOI) wafer with a device layer of 50 μm, buried oxide layer (BOX) of 3 μm and a bulk handle layer of 450 μm respectively. An oxide layer is thermally grown using wet oxidation method in front and back side of the wafer. The front side oxide layer acts as
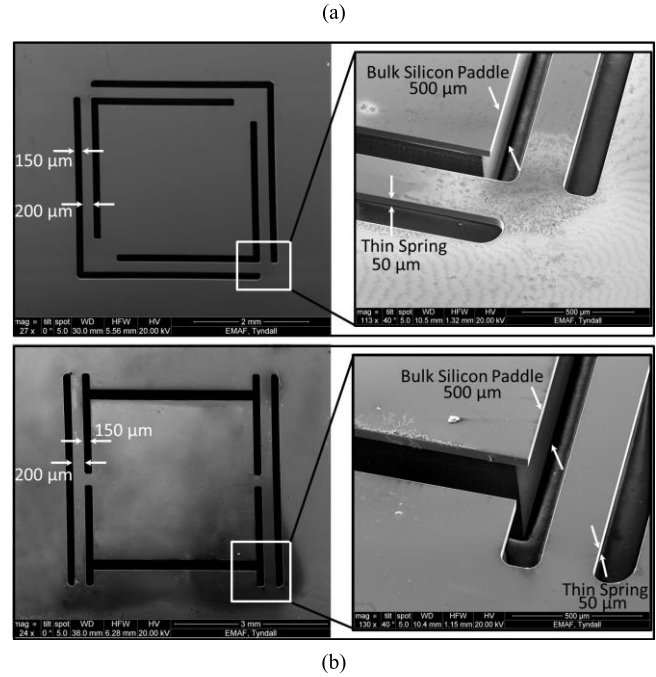

Fig. 4. SEM images of the (a) nonlinear architecture 1 (A1) and (b) nonlinear architecture 2 (A2). Inset figures show the tilted view of the fabricated spring structures identifying the thin spring arms and the bulk movable paddles.

the mask layer for the front device layer silicon etch whereas the back side oxide acts same for the back silicon etch. HiPR 6512 positive photoresist was spun on the front of the wafer, pattern was transferred using first mask and developed subsequently. The front oxide layer is etched on the exposed sites using Plasma Enhanced Reactive Ion Etching (PERIE) to reach the device layer silicon. The resist was stripped off. HiPR 6512 photoresist was spun on the back of the wafer and patterned using a second mask to etch the oxide layer for back silicon etching. After etching of the back side oxide layer, the resist was stripped off. The device layer silicon in the front is etched using Deep Reactive Ion Etching (DRIE) up to the BOX layer to define the thin spring structure. 6 μm thick Al layer is sputtered in the front to provide mechanical support to the front silicon spring layer while the back silicon and oxide is etched sequentially. The handle layer silicon in the back is then etched using DRIE technique, followed by removal of the BOX layer. The wafer is diced and sputtered Al layer is wet etched to release the mechanical structure. The Scanning Electron Microscope (SEM) images of the two spring configurations are shown in Fig. 4(a) and 4(b) respectively. The thin spring arms and bulk central paddles are identified in the tilted images in the inset figures.

The double layer electroplated copper coil is fabricated on a separate Silicon substrate [33] and the corresponding process flow is shown in Fig. 5. The fabrication process starts by sputtering Ti/Cu (20/200 nm) seed layer on silicon. The substrate is then patterned and the first layer of copper is electroplated and resist is stripped off. Using a second mask, via layer is patterned and copper is again electroplated to fill the via. Next, SU-8 insulation layer is spun to isolate the bottom copper tracks from the top layer. Similar seed layers (Ti/Cu) as the bottom is sputtered again on SU-8. The
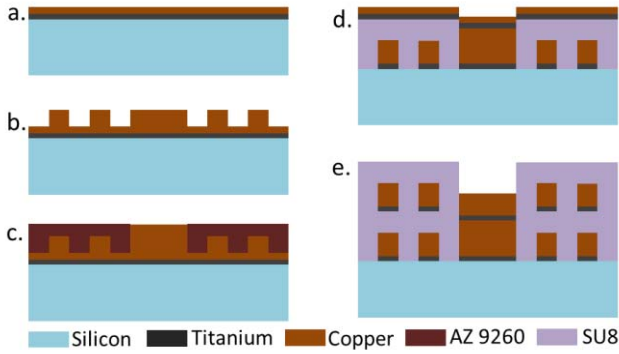
Fig. 5. Process flow for fabrication of double layer electroplated copper coil: (a) Si substrate with sputtered Ti/Cu seed layer; (b) bottom layer of coil deposition; (c) via layer deposition; (d) SU-8 insulation layer spin coated; (e) top layer coil deposition.
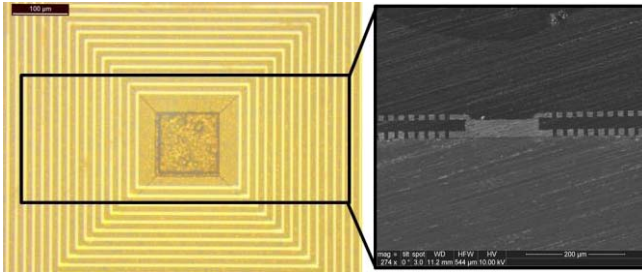

Fig. 6. Optical image of the fabricated micro-coil from the top. The SEM image of the cross-section of the coils is shown as inset. The two layers of coppers are clearly visible there.

TABLE II

Comparison Between Micro-Fabricated and Commercially Available Copper Coils

Coil	No. of turns	Area (cm^2)	Thickness (mm)	Resistance (Ω)
Wire Wound	560	0.08	0.5	140
Micro-fabricated	144	0.09	0.03	192

corresponding layer is patterned before top layer copper is electroplated and the resist is stripped off. Finally another layer of SU-8 is spun to provide passivation to the structure. Optical image of a portion of the micro coil is shown in Fig. 6 and cross-sectional image using SEM is shown in the inset which clearly shows the two conductive copper layers of the coil connected at the middle. A comparison between the micro-fabricated coil and the wire wound coil of similar dimension is provided in Table II. At the packaging stage, the magnets are manually epoxy bonded on the silicon paddle under the optical microscope. In the manual procedure, it is difficult to guarantee an exact alignment of the center of the magnet with that of the coil below. However, it is observed using finite element analysis that the slight mismatch between the centers of magnet and coil does not affect the generated output significantly.

C. Electro-Mechanical Model

According to Faraday's law, the induced voltage in the coil is proportional to the negative rate of change of magnetic flux through the coil. Using simulations in COMSOL Multiphysics, the relationship between the magnetic flux density (B)
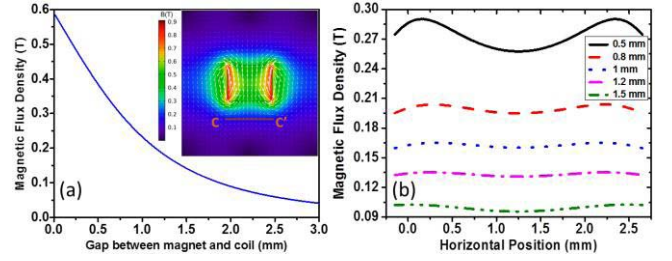

Fig. 7. (a) Magnetic flux density along the axis passing through the center of the magnets. The inset shows the magnetic flux line distribution with respect to the rest position of the coil (CC'). (b) Magnetic flux distribution over the plane of the coil for different gaps between the magnet and the coil.

and the gap (z) between the magnet and coil along the center line of the magnet is shown in Fig. 7(a), where B decreases with increase in the gap distance. At a gap distance of 1 mm, a magnetic flux density of 0.23 T is obtained by assuming the residual magnetic flux density (Br) of 1.4 T for the NdFeB N52 magnets. The inset figure shows the magnetic flux line distribution along the cross-section. The simulation shows that the magnetic flux density is mostly concentrated near the surface of the magnet and decreases drastically away from the magnet. However, to allow the movement of the magnets the gap should be adjusted according to the maximum amplitude of the displacement of the magnets. In our design, the coil experiences the variation from dense to sparse magnetic field due to the relative motion between the magnet and coil which creates the desired flux gradient. The variation of the static magnetic flux density along the plane of the coil for different distances between the magnet and coil is shown in Fig. 7(b). The change of the slope near the edge of the coil is due to the fact that the width of the coil is greater than that of the magnet. We have used the same electromagnetic assembly throughout our study for consistency with different nonlinear springs.

In a fixed-free configured beam, there is only linear bending strain. But in a specifically designed fixed-fixed beam, an additional stretching strain is obtained in addition to the bending strain. The resultant spring force (F) of such specially designed beams consists of two parts, one due to bending (F_b) and the other due to stretching (F_S) which is given by [31]

$$F = F_b + F_s = -\left(\frac{Y}{L^3}Wd^3\right)d_f - (\frac{18}{25}\frac{Y}{L^3}Wd)d_f^3 \qquad (1)$$

Where, L, W, d and Y are length, width, thickness and Young's modulus of the beam and d_f is the beam tip deflection. For small amplitude oscillations ($d_f < d$) when tip deflection is less than the thickness of the beam, the second term on the right hand side of equation (1) is insignificant and deflection consists of bending strain dominantly. However for large deflection when amplitude of oscillation is comparable or greater than the thickness of the beam ($d_f \geq d$), the stretching effect becomes dominant and nonlinearity plays pivotal role in the response of the devices. This nonlinearity ultimately results in wideband output response of the devices. It is understood from equation (1) that the thickness of the spring arms is an important parameter for designing this kind of stretching induced nonlinear architectures i.e., smaller the thickness of

This article has been accepted for inclusion in a future issue of this journal. Content is final as presented, with the exception of pagination.

MALLICK *et al.*: HIGH FIGURE OF MERIT NONLINEAR MICROELECTROMAGNETIC ENERGY HARVESTERS
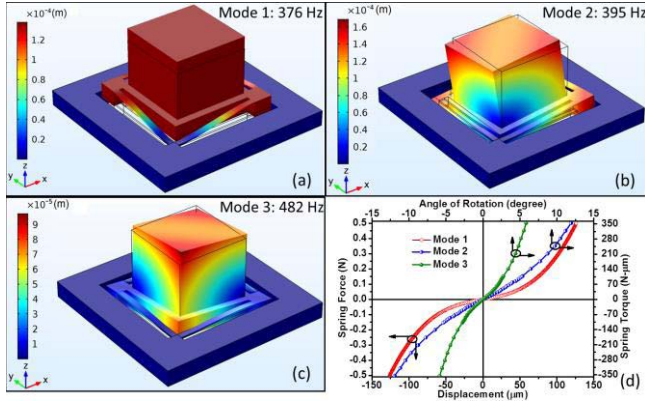5

Fig. 8. First three fundamental modes of A1 from COMSOL: (a) Vertically up and down movement at 376 Hz, (b) Torsional motion at 395 Hz, (c) Another torsion at 482 Hz. (d) Variation of spring force vs. deflection for mode 1 and spring torque vs. angular rotation for other modes of vibration respectively.
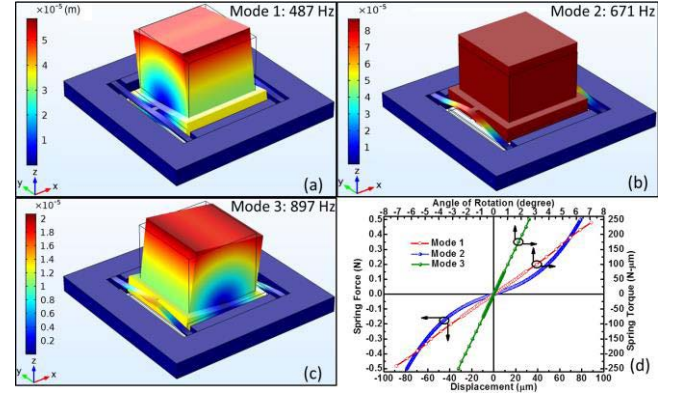

Fig. 9. First three fundamental modes of A2 from COMSOL: (a) Torsional movement at 487 Hz, (b) Vertically up and down movement at 671 Hz, (c) Twisting movement at 897 Hz. (d) Variation of spring force vs. deflection for mode 2 and spring torque vs. angular rotation for vibrational modes 1 and 3 respectively.

the spring arms, greater will be the nonlinearity. Thus this method of introducing nonlinearity into the system is one of the most convenient one for micro-fabricated energy harvesting devices as it is comparatively easy to manufacture very thin beam structures on SOI using standard MEMS processing technologies. Though such thinning of the spring arms is also restricted by process technologies such as clamping issues during dry etching of the bulk silicon etc. In our devices the thickness of the spring arms are chosen to be 50 μm.

As shown in Fig. 8(a-c), the first three vibrating modes of A1 are at 376 Hz, 395 Hz and 482 Hz respectively where the device undergoes vertical deflection and torsion along different directions. The closely spaced fundamental modes help in improving the wideband characteristic of the nonlinear springs. In linear resonator based systems, multi modal design is a common approach to harness energy from different vibration frequency peaks; whereas the nonlinear effect associated with different vibration modes and their potential interactions producing even enhanced wideband response is unreported and hence not analyzed properly. The nonlinear behavior of the different modes of A1 can be understood from Fig. 8(d). The spring force variation in case of the first mode is shown as a function of the displacement whereas the variation of the produced spring torque as a function of the angular rotations of mode 2 and 3 are shown using FEM analysis in COMSOL Multiphysics. Using small angle approximation, the angular rotations are calculated from the deflection values in Comsol for different applied torques. The nonlinearity produced at the large deflections can be easily observed from the plots. For the mode 1, the spring force variation is almost in the linear regime till 50 μm. Beyond this point the spring force enters the nonlinear regime as the stretching strain becomes significant.

The first three fundamental modes of A2 are at 487 Hz, 671 Hz and 897 Hz respectively as shown in Fig. 9(a-c). These modes correspond to torsional, vertical and twisting motions. Ideally one would like to have the vertical up-down motion as the first mode as that should be the most dominating mode of the spring architecture as that would maximize the magnetic flux linkage. But in this case the torsional motion is obtained at lower frequency due to the presence of the thin beam joints as

indicated in Fig. 1(b) which makes the torsion easier compared to A1 where the beam joints are bulk [Fig. 1(a)]. In A2, the gap between different modes is quite wide compared to that in A1. Also it is observed from Fig. 9(d) that except the vertically moving mode 2, other modes do not incorporate any nonlinear effect. Hence, the influence of the interaction between different degrees-of-freedoms is expected to be lower. It is observed that both linear and nonlinear stiffness for vertical mode A2 is higher compared to that of A1. Thus much higher force is required to produce the same deflection in A2. However as the nonlinear stiffness is higher for A2, the frequency widening effect due to nonlinear stretching of a single vibration mode is expected to be higher. The higher stiffness leads to higher operating frequency as well.

The nonlinear restoring spring force (F) described in equation (2) gives rise to Duffing potential of the form $U = \frac{1}{2}kx^2 + \frac{1}{4}k_nx^4$, where x is the displacement of the oscillator, k and k_n are the linear and nonlinear stiffness constants respectively. The derived linear and nonlinear stiffness constants of A1 and A2 spring architectures are given in Table III. The dynamical behavior of a single degree of freedom, nonlinear Duffing oscillator based electromagnetic energy harvesting devices can be described using a second order spring mass damper system incorporating the nonlinear term as

$$m\ddot{x} + \left(c_m + \frac{\gamma^2}{(R_C + R_L)}\right)\dot{x} + \frac{dU}{dx} = -m\ddot{z} \qquad (2)$$

Where, m is the proof mass, c_m is the mechanical damping co-efficient, γ is the electromagnetic coupling co-efficient and R_C, R_L are the coil and load resistances respectively.

TABLE III
COMPARISON BETWEEN STIFFNESS PARAMETERS OF THE
TWO NONLINEAR ARCHITECTURE

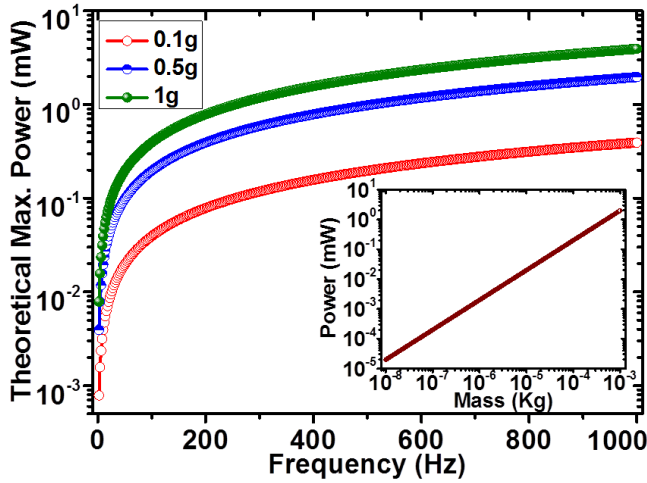| Stiffness Constant	Nonlinear Architecture 1 (A1)	Nonlinear Architecture 2 (A2)
Linear Stiffness (k) (N/m)	917.2	2665.7
Nonlinear Stiffness (k_n) (N/m^3)	1.93×10^{11}	5.62×10^{11}

Fig. 10. Theoretical maximum average power from the devices is plotted for different input accelerations as a reference of the actual performance. The dependence of proof mass on output power at a particular frequency (500 Hz) is shown as an inset.

Theoretically the upper boundary of the maximum obtainable power from an nonlinear energy harvesting device was calculated by Ramlan *et al*. [34] and is given as

$$P_n = \frac{2m\omega^3 Z X_{max}}{\pi} \qquad (3)$$

Where ω and Z are the angular frequency and amplitude of the input harmonic vibration and X_{max} is the maximum displacement of the oscillator under any circumstances. Since the essential features like proof mass and maximum allowable displacements of the different nonlinear energy harvesting devices are same in our case, the theoretical maximum average output power is plotted in Fig. 10 as a reference over a frequency range of 0 – 1000 Hz under different input accelerations from 0.1g to 1g (1g = 10 m/s^2). From equation (3), it is clear that proof mass plays an important role in increasing the output power. The effect of changing the mass on output power at a fixed frequency (500 Hz) is shown on the inset of Fig. 10, while keeping the other parameters unchanged. However, the actual performance of the reported devices is limited by a number of factors like parasitic damping, stiffness of the springs etc.

III. EXPERIMENTAL RESULTS & DISCUSSIONS

A. Experimental Procedure

The wideband behaviour of the fabricated devices is tested under different peak acceleration levels. The experimental test set up consists of a Brüel & Kjær LDS V455 Permanent Magnet Shaker, a LDS Comet USB vibration control system, a LDS PA 1000L power amplifier. The vibration controller produces sweeping sinusoidal signal via the power amplifier to get a constant input acceleration level which is monitored by a miniature piezoelectric CCLD accelerometer (LDS 4394). The shaker vibrates vertically in order to excite the out-of-plane (perpendicular to the plane of the device) modes. The output response from the different devices is recorded using a digital oscilloscope.

We have characterized the two MEMS nonlinear spring architectures as shown in Fig. 1 each with two different coils, wire wound and micro-fabricated coils respectively. In our study, we use the following terminologies. A1WC refers to the device in which first nonlinear architecture (A1) [Fig. 1(a)] is assembled with the wire wound coil and A1MC is the device in which the same architecture is assembled with the micro-fabricated coil. Similarly for the second nonlinear architecture (A2) [Fig. 1(b)], notations are A2WC and A2MC respectively. However in all of these cases, the NdFeB magnet (epoxy bonded onto the central paddle of the springs) acts as the proof mass, which increases the energy transduction efficiency due to the large mass of the magnet as compared to the conventional MEMS based approaches where a coil proof mass is used. The spring architectures A1 and A2 are characterized at different acceleration levels to obtain comparable outputs. As already explained, A2 is much stiffer compared to A1. Therefore, much stronger force is required to enter the nonlinear regime for A2 spring architecture. As a consequence, high acceleration values are used to obtain significantly wider bandwidth and power output from the devices with A2 spring architecture. However, 0.5g is used as a common acceleration to compare the performance of the two different spring designs.

B. Characterization of Nonlinear Architecture 1 (A1)

The load power response of the devices A1WC and A1MC as a function of the input excitation frequency for both up- and down-sweeps are shown in Fig. 11(a) and Fig. 11(b) respectively under different acceleration levels. As mentioned in section II, the first three fundamental modes of nonlinear design A1 are relatively closely spaced at 376 Hz, 395 Hz and 482 Hz. The large deflection, stretching strain nonlinearity is resulted for the out-of-plane and different tilting vibration modes of the spring architecture which leads to nonlinear output response at each mode. The first mode (376 Hz), which constitutes of the vertically up-down movement, is most dominant as the external excitation is also aligned along that direction. Also, the nonlinear contribution due to this mode is quite large as seen from Fig. 8(d). With increase of input excitation frequency, the nonlinear contribution due to the following modes compliance with the first mode and that adds up to the overall nonlinear output response of the device. As a result, ultra-wide output response is achieved and the corresponding wideband nature escalates with the increase of input acceleration. Similar frequency response is observed for both A1WC and A1MC as the same nonlinear spring architecture is used for both. The inset of Fig. 11(a) shows the open circuit voltage response of A1WC at a low acceleration of 0.02g where only the vertically moving first mode is significant whereas other modes are not recognizable. The peak is obtained at 367 Hz which agrees fairly well with the FEM analysis (376 Hz). As seen from the experiments, maximum load power is generated for both the prototypes when the internal coil resistance is equal to the external load resistance. This condition holds when the parasitic damping is higher compared to the electrical damping. In MEMS based
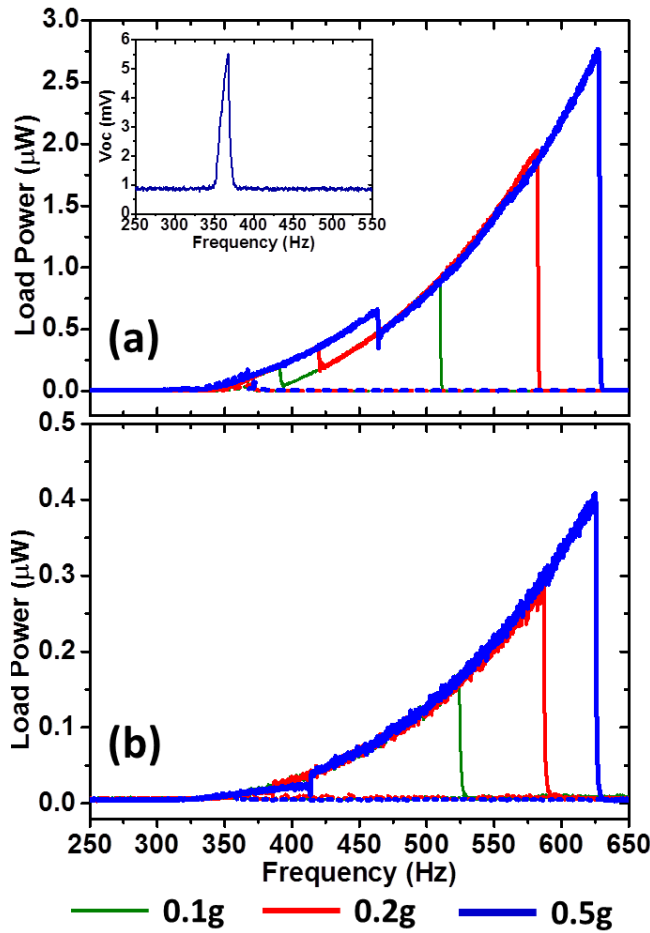
This article has been accepted for inclusion in a future issue of this journal. Content is final as presented, with the exception of pagination.

MALLICK *et al.*: HIGH FIGURE OF MERIT NONLINEAR MICROELECTROMAGNETIC ENERGY HARVESTERS 7

Fig. 11. Measured load power response of (a) A1WC and (b) A1MC as a function of input frequency for various accelerations for both up- and down-sweep of the frequency. The inset in (a) shows the open circuit voltage response of A1 at low acceleration of 0.02g.
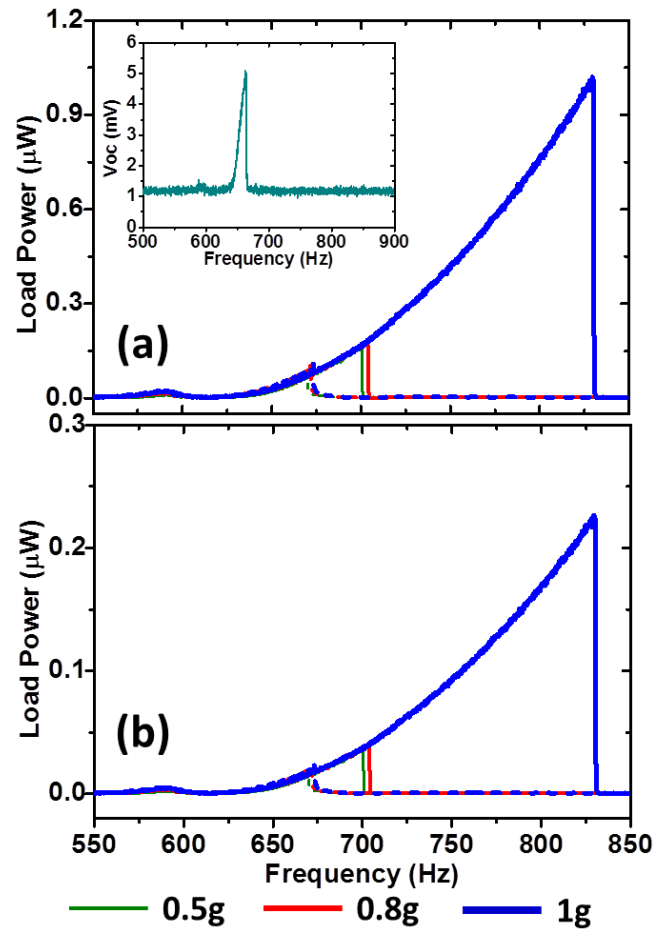

Fig. 12. Measured load power response of (a) A2WC and (b) A2MC as a function of input frequency for various accelerations for both up- and down-sweep of the frequency. The inset in (a) shows the open circuit voltage response of A2 at low acceleration of 0.1g.

electromagnetic generators, the electrical damping is expected to be low as the small dimension magnet and coil assembly produces relatively lower electromagnetic coupling and there is little scope to form efficient magnetic arrangements, which affects the output power also. Thus the optimized load for both the devices are equal to the respective coil resistances i.e., for AIWC it is 140 Ω and for A1MC the same is 190 Ω respectively. At 0.5g, the maximum average load power of 2.87 μW is obtained at the jump-down frequency of 629 Hz with a half power bandwidth of 82 Hz. Peak load power of 0.41 μW is generated at 627Hz for A1MC along with a bandwidth of 80 Hz at 0.5g input acceleration. The significant fall of output power for A1MC compared to that of A1WC is due to the low electrical damping produced from the microfabricated coil with less coil turn numbers than the wire wound coil, whereas the output bandwidth remain almost same due to the identical mechanical structures.

C. Characterization of Nonlinear Architecture 2 (A2)

Similarly load power variations of the devices A2WC and A2MC with up- and down-sweep of input frequency are shown in Fig. 12(a) and Fig. 12(b) under three different acceleration levels such as 0.5g, 0.8g and 1g. It is

observed from FEM analysis in the previous section that the first vibration mode (487 Hz) of this spring structure is torsional mode which is relatively linear whereas the second vertically moving mode at 671 Hz is nonlinear in nature. Thus for devices with A2 architecture, no overlap between wideband responses occur. A linear peak is obtained near 587 Hz, -generating 0.023 μW at the peak for A2WC and 0.0054 μW for A2MC. However, such resonant response is followed by the wideband output frequency response due to the strong nonlinearity of the second vibrational mode. Like the previous case, the output response also widens with the increase of input acceleration. The jump-down frequency for this strong nonlinear response increases significantly from 700 Hz at 0.5g to 704 Hz at 0.8g and 829 Hz at 1g. This can be explained from the spring force variation with displacement of the corresponding mode shown in Fig. 10(d). As compared to A1, much higher force is needed for A2 to enter in the sufficiently nonlinear regime. Thus, larger input accelerations are needed to achieve the desired wideband output. At 1g acceleration, maximum load power of 1.05 μW is generated for A2WC at 829 Hz. The corresponding half power bandwidth of the device is 60 Hz. On the other hand, maximum load power of 0.22 μW is produced for the

This article has been accepted for inclusion in a future issue of this journal. Content is final as presented, with the exception of pagination.

8

JOURNAL OF MICROELECTROMECHANICAL SYSTEMS

TABLE IV

COMPARISON OF POWER INTEGRAL FOR DIFFERENT REPORTED MEMS NONLINEAR ENERGY HARVESTERS WITH OUR WORK

Reference	Type of Transduction	Volume (cm^3)	Acceleration (g)	NB*	Output Power (μW)	Power Integral (μW-Hz)	NPID (kg/m^3)
[7]	EM (MEMS Spring and coil)	0.158	1g	0.16	0.59 X 10^{-4}	0.02	0.0013
[28]	EM (MEMS Spring and coil)	0.032	3g	0.018	0.002	1.8	0.0625
[15]	EM (MEMS Spring and coil)	0.09	4.5g	0.16	0.82	98.4	0.54
[37]	PZ	0.016	0.6g	0.24	0.11	2.8	4.86
[11]	ES	0.042	1g (35V bias)	0.29	3.4	164	39.04
[38]	ES	0.144	0.42g (800V bias)	0.039	0.95	0.95 (approx.)	0.37
A1WC	EM (MEMS Spring)	0.14	0.5g	0.13	2.87	840	240
A1MC	EM (MEMS Spring and coil)	0.14	0.5g	0.13	0.41	123	35.14
A2WC	EM (MEMS Spring)	0.14	1g	0.07	1.05	225.75	16.13
A2MC	EM (MEMS Spring and coil)	0.14	1g	0.07	0.22	47.3	3.38

EM - Electromagnetic; PZ – Piezoelectric; ES – Electrostatic
*Frequency values are approximated from figure unless mentioned explicitly

device A2MC under similar excitation condition at 830 Hz which corresponds to a half power bandwidth of 61 Hz. In this case also the load resistances of both the prototypes are adjusted to match the respective coil resistances for optimal power generation. It is to be noted that both the load power and the half power bandwidth of the prototypes with the A2 nonlinear structures are comparatively smaller than those of the prototypes with A1 variant. This can be attributed to the fact that A2 is much stiffer compared to A1 which imposes higher structural damping [35] as well and reduces the output power in spite of -nonlinear contribution from other modes as in the case of A1WC and A1MC.

D. Benchmarking

In this work we have reported nonlinear stretching effect based energy harvesting devices where the main motivation is to transduce electrical power efficiently from a wideband vibration source, as opposed to linear generators which are suitable for deriving power from vibrational sources with discrete frequency peaks. Thus in order to benchmark the reported devices in a more justified way, a suitable figure of merit is required as opposed to conventional figure of merits such as 'normalized power density' which are more suitable for linear resonant generators as they consider only the output power at the resonance frequency. As a figure of merit for wideband energy harvesters, the concept of 'power integral' is introduced before [36]. The power integral is the area under the load power-frequency curve at a fixed acceleration level and is defined as $(P_f = \int P_L df)$ where P_L is the load power and f is the frequency. A generalized figure of merit, 'Normalized Power Integral Density (NIPD)', can be obtained by normalizing P_f w.r.t the volume of the device and the input

accelerations, which can be defined as

$$Normalized\ Power\ Integral\ Density\ (NPID)$$
$$= \frac{P_f}{Volume.Acceleration^2} \quad (4)$$

In micro fabricated energy harvesting devices, the output power is normally significantly reduced due to the scaling of the active material whereas the bandwidth increases due to the larger nonlinearity because of the thinner spring structures. In the Table IV, we provide a comparative study of the reported MEMS based wideband energy harvesting devices along with our work. As various devices operate at different frequencies, direct comparison of their bandwidth is also not justified. Therefore we derive 'normalized bandwidth' which is defined as

$$Normalized\ Bandwidth\ (NB) = \frac{Bandwidth}{Peak\ Power\ Frequency} \quad (5)$$

For nonlinear energy harvesters, the peak power frequency is normally same as the jump down frequency during up sweep. Since the operational bandwidth depends on the working frequency of the devices, the normalized bandwidth provides a fair comparison between the performances of different devices. The efficient nonlinear spring design in our device produces sufficient wideband response, which results in comparable normalized bandwidth and large power integral values. However as shown in Fig. 10, the performance can be improved by further optimizations. Another concern that can be raised is the relatively high frequency of operation of the reported devices whereas most of the available vibration sources are low frequency (<100 Hz). However, there are a number of application scenarios where

This article has been accepted for inclusion in a future issue of this journal. Content is final as presented, with the exception of pagination.

MALLICK *et al.*: HIGH FIGURE OF MERIT NONLINEAR MICROELECTROMAGNETIC ENERGY HARVESTERS

9

the available mechanical energy is located in the moderately high frequency (100-1000 Hz) region. In case of tire pressure monitoring system (TPMS), the vibration is distributed over the frequency range from 100 to 1000 Hz with quite high acceleration [39]. Similar high frequency application environment is available from aerospace vehicles during their take-off and landing [40]. The reported devices can be useful under such circumstances for harvesting useful electrical energy.

IV. Conclusions

We report wideband MEMS electromagnetic energy harvesters employing two different nonlinear spring architectures. Nonlinearity is introduced in the spring structures by the stretching in addition to bending of the specially designed fixed-fixed configured spring arms and this gives rise to a wideband output response. In first nonlinear architecture (A1), the fixed ends are orthogonal to each other with beam joint in the middle whereas the second nonlinear architecture (A2) is H-shaped. The realization of the spring architectures on the thin Silicon-on-Insulator substrate using MEMS processing technology activate different fundamental modes of the devices which further widens the output response. The devices are characterized at different level of MEMS integration to report a comparative result. Experimental results show that around 80 Hz of half power bandwidth is obtained for devices with A1 architectures due to nonlinear contributions from closely spaced vibration modes. On the other hand, devices with A2 spring structures have 60 Hz half power band width due to strong nonlinear stiffness of the beams. The devices are benchmarked using 'power integral (P_f)' figure-of-merit, which shows that the efficient nonlinear designs result in a high P_f values compared to the reported MEMS electromagnetic energy harvesting devices.

Acknowledgment

References

[1] S.-H. Yang, "Internet of Things," in *Wireless Sensor Networks*. New York, NY, USA: Springer, 2014, pp. 247–261.

[2] C. Perera, A. Zaslavsky, P. Christen, and D. Georgakopoulos, "Sensing as a service model for smart cities supported by Internet of Things," *Trans. Emerg. Telecomm. Technnol.*, vol. 25, no. 1, pp. 81–93, Jan. 2014.

[3] A. Erturk and D. J. Inman, "An experimentally validated bimorph cantilever model for piezoelectric energy harvesting from base excitations," *Smart Mater. Struct.*, vol. 18, no. 2, p. 025009, 2009.

[4] R. Elfrink *et al.*, "Vibration energy harvesting with aluminum nitride-based piezoelectric devices," *J. Micromech. Microeng.*, vol. 19, no. 9, p. 094005, 2009.

[5] A. Hajati and S.-G. Kim, "Ultra-wide bandwidth piezoelectric energy harvesting," *Appl. Phys. Lett.*, vol. 99, no. 8, p. 083105, 2011.

[6] S. Kulkarni *et al.*, "Design, fabrication and test of integrated micro-scale vibration-based electromagnetic generator," *Sens. Actuators A, Phys.*, vols. 145–146, pp. 336–342, Jul./Aug. 2008.

[7] H. Liu, K. H. Koh, and C. Lee, "Ultra-wide frequency broadening mechanism for micro-scale electromagnetic energy harvester," *Appl. Phys. Lett.*, vol. 104, no. 5, p. 053901, 2014.

[8] S. P. Beeby *et al.*, "A micro electromagnetic generator for vibration energy harvesting," *J. Micromech. Microeng.*, vol. 17, no. 7, pp. 1257–1265, 2007.

[9] P. D. Mitcheson, P. Miao, B. H. Stark, E. M. Yeatman, A. S. Holmes, and T. C. Green, "MEMS electrostatic micropower generator for low frequency operation," *Sens. Actuators A, Phys.*, vol. 115, nos. 2–3, pp. 523–529, Sep. 2004.

[10] S. D. Nguyen and E. Halvorsen, "Nonlinear springs for bandwidth-tolerant vibration energy harvesting," *J. Microelectromech. Syst.*, vol. 20, no. 6, pp. 1225–1227, Dec. 2011.

[11] P. Basset *et al.*, "Electrostatic vibration energy harvester with combined effect of electrical nonlinearities and mechanical impact," *J. Micromech. Microeng.*, vol. 24, no. 3, p. 035001, Feb. 2014.

[12] Y. Jiang *et al.*, "Fabrication of a vibration-driven electromagnetic energy harvester with integrated NdFeB/Ta multilayered micro-magnets," *J. Micromech. Microeng.*, vol. 21, no. 9, pp. 095014-1–095014-6, 2011.

[13] M. Han, Q. Yuan, X. Sun, and H. Zhang, "Design and fabrication of integrated magnetic MEMS energy harvester for low frequency applications," *J. Microelectromech. Syst.*, vol. 23, no. 1, pp. 204–212, Jan. 2014.

[14] Q. Zhang and E. S. Kim, "Micromachined energy-harvester stack with enhanced electromagnetic induction through vertical integration of magnets," *J. Microelectromech. Syst.*, vol. 24, no. 2, pp. 384–394, Apr. 2015.

[15] Q. Zhang and E. S. Kim, "Microfabricated electromagnetic energy harvesters with magnet and coil arrays suspended by silicon springs," *IEEE Sensors J.*, vol. 16, no. 3, pp. 634–641, Feb. 2016, doi: 10.1109/JSEN.2015.2487994.

[16] Ö. Zorlu and H. Külah, "A MEMS-based energy harvester for generating energy from non-resonant environmental vibrations," *Sens. Actuators A, Phys.*, vol. 202, pp. 124–134, Nov. 2013.

[17] S. E. Leland and P. K. Wright, "Resonance tuning of piezoelectric vibration energy scavenging generators using compressive axial preload," *Smart Mater. Struct.*, vol. 15, no. 5, pp. 1413–1420, 2006.

[18] V. R. Challa, M. G. Prasad, Y. Shi, and F. T. Fisher, "A vibration energy harvesting device with bidirectional resonance frequency tunability," *Smart Mater. Struct.*, vol. 17, no. 1, p. 015035, 2008.

[19] D. Mallick and S. Roy, "Bidirectional electrical tuning of FR4 based electromagnetic energy harvesters," *Sens. Actuators A, Phys.*, vol. 226, pp. 154–162, May 2015.

[20] A. Cammarano, S. G. Burrow, D. A. W. Barton, A. Carrella, and L. R. Clare, "Tuning a resonant energy harvester using a generalized electrical load," *Smart Mater. Struct.*, vol. 19, no. 5, p. 055003, 2010.

[21] I. Sari, T. Balkan, and H. Kulah, "An electromagnetic micro power generator for wideband environmental vibrations," *Sens. Actuators A, Phys.*, vols. 145–146, pp. 405–413, Jul./Aug. 2008.

[22] B. Yang *et al.*, "Electromagnetic energy harvesting from vibrations of multiple frequencies," *J. Micromech. Microeng.*, vol. 19, no. 3, pp. 035001-1–035001-8, 2009.

[23] H. Liu, Y. Qian, and C. Lee, "A multi-frequency vibration-based MEMS electromagnetic energy harvesting device," *Sens. Actuators A, Phys.*, vol. 204, pp. 37–43, Dec. 2013.

[24] F. Cottone, H. Vocca, and L. Gammaitoni, "Nonlinear energy harvesting," *Phys. Rev. Lett.*, vol. 102, p. 080601, Feb. 2009.

[25] S. C. Stanton, C. C. McGehee, and B. P. Mann, "Nonlinear dynamics for broadband energy harvesting: Investigation of a bistable piezoelectric inertial generator," *Phys. D, Nonlinear Phenomena*, vol. 239, no. 10, pp. 640–653, May 2010.

[26] A. Erturk, J. Hoffmann, and D. J. Inman, "A piezomagnetoelastic structure for broadband vibration energy harvesting," *Appl. Phys. Lett.*, vol. 94, no. 25, pp. 254102-1–254102-3, Jun. 2009.

[27] B. P. Mann and N. D. Sims, "Energy harvesting from the nonlinear oscillations of magnetic levitation," *J. Sound Vibrat.*, vol. 319, nos. 1–2, pp. 515–530, Jan. 2009.

[28] H. Liu, Y. Qian, N. Wang, and C. Lee, "An in-plane approximated nonlinear MEMS electromagnetic energy harvester," *J. Microelectromech. Syst.*, vol. 23, no. 3, pp. 740–749, Jun. 2014.

[29] B. Marinkovic and H. Koser, "Smart sand—A wide bandwidth vibration energy harvesting platform," *Appl. Phys. Lett.*, vol. 94, no. 10, p. 103505, 2009.

[30] S. C. Stanton, C. C. McGehee, and B. P. Mann, "Reversible hysteresis for broadband magnetopiezoelastic energy harvesting," *Appl. Phys. Lett.*, vol. 95, no. 17, p. 174103, 2009.

[31] D. Mallick, A. Amann, and S. Roy, "A nonlinear stretching based electromagnetic energy harvester on FR4 for wideband operation," *Smart Mater. Struct.*, vol. 24, no. 1, p. 015013, 2015.

[32] Y. Lu, F. Cottone, S. Boisseau, F. Marty, D. Galayko, and P. Basset, "A nonlinear MEMS electrostatic kinetic energy harvester for human-powered biomedical devices," *Appl. Phys. Lett.*, vol. 107, no. 25, p. 253902, 2015.

[33] P. Podder, P. Constantinou, D. Mallick, and S. Roy, "Silicon MEMS bistable electromagnetic vibration energy harvester using double-layer micro-coils," *J. Phys, Conf. Ser.*, vol. 660, no. 1, p. 012124, 2015.

[34] R. Ramlan, M. J. Brennan, B. R. Mace, and I. Kovacic, "Potential benefits of a non-linear stiffness in an energy harvesting device," *Nonlinear Dyn.*, vol. 59, no. 4, pp. 545–558, 2010.

[35] R. Pratap, S. Mohite, and A. K. Pandey, "Squeeze film effects in MEMS devices," *J. Indian Inst. Sci.*, vol. 87, no. 1, pp. 75–94, 2007.

[36] D. Mallick, A. Amann, and S. Roy, "Interplay between electrical and mechanical domains in a high performance nonlinear energy harvester," *Smart Mater. Struct.*, vol. 24, no. 12, p. 122001, 2015.

[37] H. Liu, C. Lee, T. Kobayashi, C. J. Tay, and C. Quan, "Investigation of a MEMS piezoelectric energy harvester system with a frequency-widened-bandwidth mechanism introduced by mechanical stoppers," *Smart Mater. Struct.*, vol. 21, no. 3, p. 035005, 2012.

[38] K. Tao, S. W. Lye, J. Miao, L. Tang, and X. Hu, "Out-of-plane electret-based MEMS energy harvester with the combined nonlinear effect from electrostatic force and a mechanical elastic stopper," *J. Micromech. Microeng.*, vol. 25, no. 10, p. 104014, 2015.

[39] M. Löhndorf, T. Kvisterøy, E. Westby, and E. Halvorsen, "Evaluation of energy harvesting concepts for tire pressure monitoring systems," in *Proc. PowerMEMS*, Freiburg, Germany, 2007, pp. 331–334.

[40] M. R. Pearson, M. J. Eaton, R. Pullin, C. A. Featherston, and K. M. Holford, "Energy harvesting for aerospace structural health monitoring systems," *J. Phys., Conf. Ser.*, vol. 382, no. 1, p. 012025, 2012.

Andreas Amann received the Ph.D. degree in physics from the Technical University of Berlin, Berlin, Germany, in 2003. He was a Post-Doctoral Researcher at the Technical University of Berlin. He was a Visiting Researcher at the National Institute of Applied Optics, Florence, Italy. He joined the Tyndall National Institute, University College Cork, Cork, Ireland, in 2005. Since 2010, he has been a Lecturer with the School of Mathematical Sciences, University College Cork. His research interests include the mathematical modeling of physical devices and the application of nonlinear dynamics to problems in photonics, electronics, and mechanics.

Dhiman Mallick was born in Kolkata, India, in 1986. He received the B.Tech. and M.Tech. degrees in radio physics and electronics engineering from the University of Calcutta, Kolkata, in 2010 and 2012, respectively. He joined the Tyndall National Institute, University College Cork, Ireland, in 2012, as a Ph.D. Research Student and currently holding that position. He received the UCC Strategic Research Fund Ph.D. studentship Award in 2014 by University College Cork. His research interests include vibrational energy harvesting, MEMS-based energy harvesters, magnetic thin films and nanostructures, and MEMS-based actuators.

Saibal Roy (M'12) received the M.Sc. degree in physics from the IIT and the Ph.D. degree from IACS, India. He is currently a Science Foundation Ireland Principal Investigator and also the Head of the Micropower Systems and Nanomagnetics, Tyndall National Institute, Ireland. His professional experiences include 18 years academic and three years industrial experience as the Head of research groups. In 2013, he was hosted by the Electrical Engineering Department, Stanford University, on a sabbatical visit. He holds three patents. He has authored or co-authored seven book chapters and over 160 papers in journals and peer-reviewed conference proceedings with h-index of 27. His current research interests include investigating how engineered nanostructures could be employed for the benefits of micron scale devices. He received the prestigious Visiting Chair Professorship in Engineering (Prof A S Paintal Chair) by the Indian National Science Academy, Govt. of India, in 2015.